Journal of Power Sources 206 (2012) 236–244

Contents lists available at SciVerse ScienceDirect

Journal of Power Sources

journal homepage: www.elsevier.com/locate/jpowsour

Lithium metal electrode kinetics and ionic conductivity of the solid lithium ion conductors "$Li_7La_3Zr_2O_{12}$" and $Li_{7-x}La_3Zr_{2-x}Ta_xO_{12}$ with garnet-type structure

Henrik Buschmann, Stefan Berendts, Boris Mogwitz, Jürgen Janek*

Physikalisch-Chemisches Institut, Justus-Liebig-Universität Gießen, Heinrich-Buff-Ring 58, 35392 Gießen, Germany

ARTICLE INFO

Article history:
Received 31 October 2011
Received in revised form
31 December 2011
Accepted 13 January 2012
Available online 23 January 2012

Keywords:
Lithium solid electrolyte
Cubic garnet
Ta substitution
Lithium metal electrodes
Electrode kinetics
Exchange current density

ABSTRACT

The lithium-ion solid electrolyte "$Li_7La_3Zr_2O_{12}$" (LLZO) and the tantalum substituted analogue $Li_{7-x}La_3Zr_{2-x}Ta_xO_{12}$ (LLZTO) with varying Ta content $0.375 < x < 1.5$ were prepared and structurally and electrochemically characterized. Both, LLZO and Ta substituted LLZTO were prepared by high temperature ceramic processing and were found to crystallize in the cubic garnet-type structure (space group $Ia\bar{3}d$). Phase formation was studied by X-ray powder diffraction. While Al doping was necessary for the preparation of dense LLZO ceramics crystallizing in the high lithium ion conductive cubic garnet modification, dense cubic tantalum substituted LLZTO ceramics could be prepared without Al doping. Ta substitution was found to facilitate the formation of the cubic garnet modification at lower synthesis temperature. The temperature dependence of the ionic conductivity and lithium metal electrode kinetics were studied by ac impedance spectroscopy and cyclic voltammetry, respectively. The ionic conductivity of cubic LLZTO was found to increase by Al doping. The highest room temperature conductivity of 5×10^{-4} S cm^{-1} with an activation energy of $E_a = 0.41$ eV was found for the sample $Li_{6.625}La_3Zr_{1.625}Ta_{0.375}O_{12}$ with 28 mol% Al content. Lithium electrode kinetics was studied on LLZO and LLZTO samples. The electrode activation energies of all investigated samples showed similar values between $E_a = 0.41$ eV and 0.46 eV close to the activation energies for lithium ion migration in the bulk electrolyte. Thus, the Ta substituted and Al-doped material $Li_{6.625}La_3Zr_{1.625}Ta_{0.375}O_{12}$ (29 mol% Al) showed a more than one order of magnitude higher exchange current density of $i_0 = 240$ μA cm^{-2} than Ta-free LLZO with $i_0 = 18$ μA cm^{-2}.

1. Introduction

Today, the quest for new lithium ion electrolytes suitable for the use in lithium batteries is one of the main challenges to improve established lithium ion battery performance and to enable new battery chemistry and concepts. Stable solid electrolytes with high lithium ion conductivity may help to improve present and to introduce new types of lithium batteries. In case of the so called next generation cell concepts like "lithium-air" and "lithium-sulfur" cells, a purely lithium ion conducting and otherwise impermeable separator (membrane) between anode and cathode would prevent the penetration of e.g. oxygen and moisture or soluble sulfur species ("shuttle mechanism") from the cathode to the anode side of the battery. This would be a solution to some of the major problems of these battery concepts. Furthermore, an ion conducting membrane would allow the use of different liquid electrolytes in the anode and cathode half cells, thus offering more stable interfaces and improved cell performances. Also the use of metallic lithium as anode material might become possible as dendrite penetration across the cell can be prevented by a rigid and mechanically stable solid electrolyte membrane.

In all-solid-state cells either lithium metal or indium–lithium alloys are usually the anode material combined with a solid electrolyte, which is most likely LiPON [1], and a cathode material like $LiCoO_2$. As gas phase deposition is used, the electrolyte thickness can be reduced to approx. 1 μm [2] and thus the low conductivity of LiPON in the order of 10^{-6} S cm^{-1} is not of significant consequence for the use in micro batteries (low power applications). Thinking of free-standing membranes for the use in other battery types and easier and cheaper manufacturing processes, an electrolyte membrane needs to be thicker by at least one order of magnitude so that a material with much higher lithium ion conductivity becomes indispensable. In this context, solid lithium ion conductors with garnet-type structure recently gain a lot of interest since the report of cubic $Li_7La_3Zr_2O_{12}$ by Murugan et al. [3]. This material was found to be stable vs. lithium metal and shows the so far highest room temperature lithium ion conductivity of 3×10^{-4} S cm^{-1} ($t_{Li^+} \approx 1$) among inorganic lithium ion conductive oxides. However, the synthesis of this material was found to be difficult and it was finally shown that aluminum doping is necessary to obtain dense sintered material of the cubic polymorph with high ionic conductivity [4–8]. Both, Li-NMR as well as neutron powder diffraction studies support

* Corresponding author. Tel.: +49 6419934500; fax: +49 6419934509.
E-mail address: juergen.janek@phys.chemie.uni-giessen.de (J. Janek).

0378-7753/$ – see front matter © 2012 Elsevier B.V. All rights reserved.
doi:10.1016/j.jpowsour.2012.01.094

the assumption that Al is incorporated in the garnet structure of cubic LLZO [8], but it cannot be excluded that a small amount of Al is also situated in a residual phase or in the grain boundaries. Therefore, we prefer not to include Al into the elemental formulae of the garnet phases but to denote the amount of Al doping in mol% per mol of the respective garnet material. Recently some attempts to enhance the conductivity of LLZO by doping or substitution with Ta, Nb, Si or Y have been reported [6,9–12]. Interestingly, Xie et al. report on Al-free cubic LLZO but do not present any electrical conductivity data, most probably because the material could not be sintered to dense pellets due to decomposition at temperatures above 850 °C [13].

Despite the relevance for applications, no systematic studies of the electrode/electrolyte kinetics of garnet-type materials with anode or cathode materials have been reported, apart from first cycling experiments of a Li/LLZO/$LiCoO_2$ cell [7]. Actually, only a few studies of lithium metal electrode kinetics on solid lithium ion conducting electrolytes have been reported so far at all [14–18]. Since the total cell resistance is the sum of the electrolyte bulk resistance and the anode and cathode interface resistances, the latter may have a large impact on the overall cell resistance. In particular, the lithium electrode kinetics is of substantial interest if the electrolyte is intended to be used in contact with lithium metal electrodes. Unlike the electrolyte bulk resistance the interfacial resistances are independent of the electrolyte thickness. Therefore, the interfacial resistances can only be reduced by either increasing the active interfacial area or by means to activate an otherwise resistive interface.

In the present paper we report on both measurements of the electrical conductivity of a series of new garnet-type lithium solid electrolytes and on the lithium metal electrode kinetics. In more detail, we substituted Zr in LLZO partially by Ta in conjunction with Al doping and considered phase formation, ionic conductivity as well as the polarization resistance of lithium metal electrodes. The polarization resistance was measured for LLZO and the two Ta substituted samples which show the highest ionic conductivities. The results of both, the conductivity together with the electrode kinetic measurements allow the evaluation of the garnet-type materials with respect to their potential application in solid lithium batteries using lithium metal anodes.

2. Experimental

2.1. Synthesis

The garnet phases were prepared by high temperature synthesis using LiOH (Chempur, 99%, anhydrous), ZrO_2 (Chempur, 99.9%), La_2O_3 (Chempur 99.99%, dried at 900 °C for 12 h), Ta_2O_5 (Sigma–Aldrich, 99%) and γ-Al_2O_3 in case of aluminum doping (Merck, anhydrous). The starting materials were mixed in stoichiometric amounts (10–15 wt% LiOH excess were used) and milled for 6–8 h in 2-propanol in a planetary ball mill (Fritsch, Pulverisette 5 classic line) with zirconia balls and grinding bowls at 200 rpm. All syntheses were carried out in air atmosphere and Al-free crucibles were used to avoid any unwanted Al doping of the samples. The synthesis of the γ-Al_2O_3-doped LLZO was recently described in detail elsewhere [8]. The LLZO was doped with an Al_2O_3 content of 1.7 wt% (28 mol% Al per mol $Li_7La_3Zr_2O_{12}$). The final calcination/sintering step was conducted at 1230 °C and led to LLZO with cubic garnet-type structure without any impurity phase detected by X-ray diffraction. The tantalum substituted Al-free samples $Li_{7-x}La_3Zr_{2-x}Ta_xO_{12}$ were synthesized with Ta contents of $x = 0.5$, 1.0 and 1.5. In addition one γ-Al_2O_3-doped LLZTO sample was prepared with $x = 0.375$ and an Al_2O_3 content of 1.7 wt% (29 mol% Al per mol $Li_{6.625}La_3Zr_{1.625}Ta_{0.375}O_{12}$) since Ta substitution in addition with Al_2O_3 doping was recently found to yield garnet-type materials with high ionic conductivities [10]. All the Ta substituted samples were prepared by ball milling of the starting materials followed by heating at 950 °C for 12 h. The powders were reground and heated at 1000 °C for another 12 h after which phase formation was finished. The reground powders were pelletized, isostatically pressed at 3000 bar and finally sintered at 1000 °C for 20 h.

2.2. Phase characterization

Powder X-ray diffraction was carried out on a Siemens D500 Siemens AG, now Bruker AXS in Bragg-Bretano geometry with Cu $K\alpha_{1,2}$-radiation from 10° to 90° 2θ and a step width of 0.02° 2θ. Analysis of powder diffraction patterns was carried out using the Rietveld technique implemented into the software package FullProf [19,20]. Refinements of the garnet structures were based on the structure model of cubic LLZO recently published [8]. The number of lithium atoms in the respective garnet phase depends on the degree of Ta substitution. The calculated lithium content was shared on the 24*d* and 96*h* positions according to the structure model known from Ref. [8]. Lithium atom parameters were not refined on the basis of the X-ray diffraction data as the results are not reliable. Zr on the 16*a* position was substituted by the number of Ta atoms in the respective garnet-type sample to refine the site occupations of Zr and Ta. The aluminum positions were not refined since the X-ray scattering density and the concentration of Al is too low for reliable identification of the Al atoms in the garnet-type crystal structure. XRD patterns together with extended results of the respective Rietveld refinements are included in the supplementary data.

2.3. Electrical conductivity

Conductivity measurements were carried out after vacuum drying of the sintered garnet pellets for 8 h at 100 °C. The dried pellets were exclusively handled in argon atmosphere in a glove box system (MBraun, Labmaster) with less than 0.1 ppm residual H_2O and O_2 content. Electrochemical measurements were performed with a potentiostat/galvanostat (SP-300 from Biologic Science Instruments) using the software package EC-Lab V10.11. Temperature dependent conductivity data were collected from two electrode ac impedance measurements in the frequency range from 7 MHz to 1 Hz with an amplitude of 20 mV. Lithium foil (Chemetall) was used as electrode material. The lithium foil was pressed on both sides of the pellets as shown in Fig. 1(a) and subsequently annealed on a heating plate at 170 °C for some minutes to improve contact between lithium and garnet material. The electrodes were contacted with nickel stripes and the samples were sealed in gastight pouches made of aluminized compound foil. Temperature dependent ac impedance measurements were carried out in a temperature chamber (WTL 64 Weiss Technik) in the temperature range from −40 °C to 100 °C.

2.4. Lithium/garnet electrode kinetics

The as aforementioned dried garnet samples were polished with an abrasive paper (30 μm grain size) in the glove box atmosphere to achieve a well defined "fresh" garnet surface which had not been in contact with air before. Lithium electrodes were then gas phase deposited on the polished sides by thermal evaporation in order to achieve well reproducible and intimate contact between lithium and garnet material. This deposition was carried out in a home built deposition chamber attached to a glove box so that the sample handling took place in argon atmosphere all the time. Lithium was evaporated from a heated tungsten boat (tectra) at a residual Ar chamber pressure of about 10^{-4} mbar. Deposition of the lithium

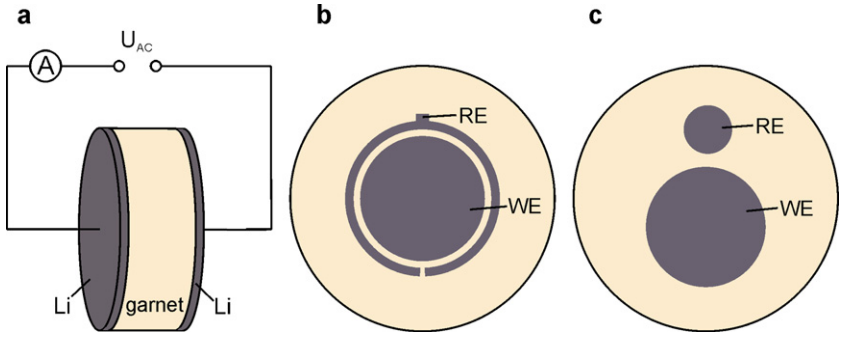

Fig. 1. Scheme of different electrode arrangements on garnet-type samples with a diameter of about 20 mm and a thickness of about 5 mm: (a) setup for ac impedance measurements with lithium electrodes; (b and c) different arrangements of working electrode (WE) and reference electrode (RE) for cyclic voltammetry measurements. *Note*: For the sake of clarity the counter electrode (same size as WE) is not illustrated in (b and c).

films was traced by a quartz crystal microbalance with a growth rate monitor (tectra). Lithium films of about 1 μm thickness were deposited.

A three electrode arrangement (WE = working electrode, CE = counter electrode, RE = reference electrode) was used as shown in Fig. 1(b). The vapor-deposited lithium electrodes were contacted with nickel stripes and the samples were finally sealed in gas-tight pouches as described before. Cyclic voltammetry (CV) at temperatures between −20 °C and 50 °C was performed with the aforementioned equipment between ±0.1 V (vs. lithium reference electrode) using a sweep rate of 1 mV s^{-1} starting with cathodic polarization. Additional galvanostatic measurements with current densities between ±400 μA cm^{-2} were performed on the $Li_{6.625}La_3Zr_{1.625}Ta_{0.375}O_{12}$ sample for comparison. The current was applied for a period of 30 s and the resulting voltage between the WE and RE was measured. The measured CVs as well as the results from galvanostatic measurements were corrected for the *IR* drop between WE and RE caused by the electrolyte resistance. This *IR* drop was determined by finite element simulations (FEM) as described in the next section.

2.5. IR drop correction – calculation of potential and current distributions by finite element method

Finite element method (FEM) simulations were used to evaluate the *IR* drop caused by the electrolyte resistance between WE and RE occurring during the Li/garnet interface kinetics measurements. The electric currents module of the COMSOL Multiphysics finite element software (version 4.2) was used for the calculations. A physics-controlled mesh was generated from about 200,000 tetrahedral elements. Additional mesh refinements were tested but did not show a significant change of the results. The default solver was used. For the calculation of the *IR* drops occurring during our measurements the exact geometries of the samples which were similar to those shown exemplarily in Fig. 1(b) and the material parameters of the respective garnet samples were used. The temperature dependence of the electrolyte resistances was included into the simulations with the experimentally determined Arrhenius-type functions of the conductivities as shown in Fig. 4.

3. Results and discussion

3.1. Sample preparation and phase formation

It is commonly known, that dense ceramic samples of the cubic garnet material "$Li_7La_3Zr_2O_{12}$" (LLZO) showing high ionic conductivity can only be prepared if the material is Al-doped [4–6], hereby stabilizing the cubic modification of LLZO due to Al^{3+} incorporation mostly on the tetragonal 24*d* lithium position [4,8]. Furthermore, Al_2O_3 doping increases the density of sintered bodies and obviously stabilizes LLZO at temperatures well above 1100 °C necessary for sintering dense ceramics. Aluminum free cubic LLZO was recently found to decompose at temperatures above 850 °C via the tetragonal phase most likely due to extensive Li_2O evaporation [13].

The tantalum substituted LLZTO with the nominal formula $Li_{7-x}La_3Zr_{2-x}Ta_xO_{12}$ could be prepared over a wide range of $x = 0.5–1.5$. All LLZTO samples crystallize in cubic garnet-type symmetry as shown in Fig. 2(a–d) without the need of stabilization by Al doping. These results are in agreement with former reported results for Nb-substituted LLZO [12]. The 29 mol% Al-doped $Li_{6.625}La_3Zr_{1.625}Ta_{0.375}O_{12}$ material also crystallizes in the cubic garnet symmetry as shown in Fig. 2(e). All Ta-substituted materials were sintered to dense ceramic samples at the comparably low temperature of 1000 °C. Fig. 2(f) shows the X-ray powder diffraction pattern of Al-doped cubic LLZO. Within the Ta substitution series the lattice parameter *a* of the resulting garnet-type materials shows a linear dependence on the Ta content as shown in Fig. 3. The substitution of the larger Zr^{4+} (86 pm, c.n. = 6) ions by the smaller Ta^{5+} (78 pm, c.n. = 6) [21,22] ions together with the simultaneous decrease of the lithium content leads to a decrease

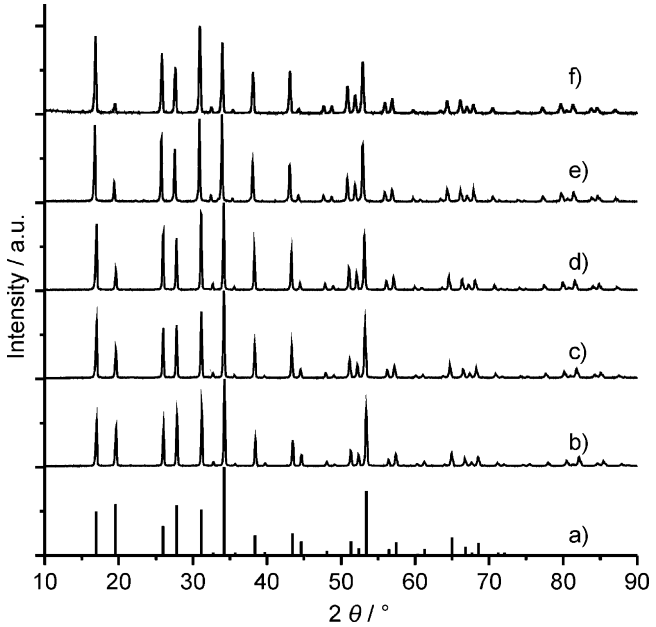

Fig. 2. Powder XRD patterns of prepared garnet-type samples (a) simulated pattern (JCPDS 45-0110), (b) $Li_{5.5}La_3Zr_{0.5}Ta_{1.5}O_{12}$, (c) $Li_6La_3ZrTaO_{12}$, (d) $Li_{6.5}La_3Zr_{1.5}Ta_{0.5}O_{12}$, (e) $Li_{6.625}La_3Zr_{1.625}Ta_{0.375}O_{12}$ (29 mol% Al), (f) $Li_7La_3Zr_2O_{12}$ (28 mol% Al) after final calcination.

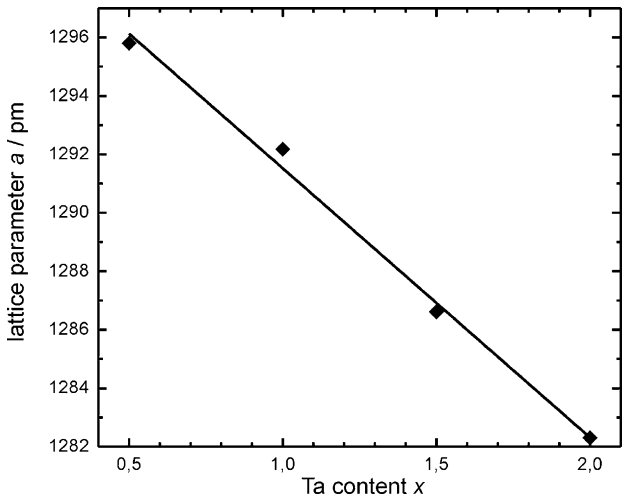

Fig. 3. Dependence of the lattice parameter a on the tantalum content x in the series of Al-free tantalum substituted $Li_{7-x}La_3Zr_{2-x}Ta_xO_{12}$ samples (the solid line represents the linear fit to the data points). The lattice parameter of $Li_5La_3Ta_2O_{12}$ was taken from Ref. [38].

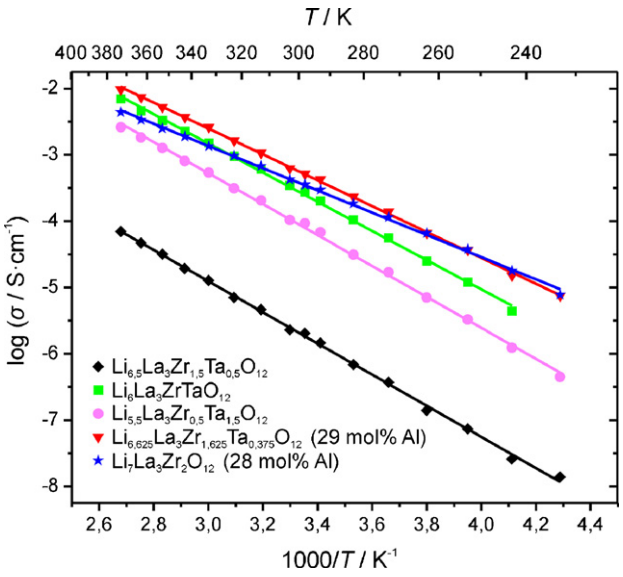

Fig. 4. Temperature dependence of the electrical conductivities of garnet-type samples with the linear fit to the data points (solid lines). *Note*: For the sake of readability $\log\sigma$ vs. $1000/T$ is shown. The activation energies given in the text were calculated from the slope of $\ln(\sigma T)$ vs. $1000/T$ remembering that $\ln(\sigma T) = \ln\sigma_0 - E_a/RT$.

of the lattice parameter with increasing Ta content. We regard this result as a proof for the substitution of Zr^{4+} by Ta^{5+} ions in the garnet lattice and it shows the miscibility of Li_2O, La_2O_3, ZrO_2 and Ta_2O_5 in the garnet-type system over the selected composition range. Results from Rietveld refinements of the Zr/Ta occupations in the different samples agreed well with the contents given by the starting material ratios. The Al-doped garnet materials have smaller unit cells than the Al free materials most likely due to the substitution of 3 Li^+ ions by one Al^{3+} ion. The lattice parameters of the Al-doped samples also decreased by Ta substitution. While the lattice parameter of Ta-free LLZO is $a = 1297.27(2)$ pm, the lattice parameter of the Ta substituted ($x = 0.375$) material is $a = 1294.38(1)$ pm. For further details of the Rietveld refinement results see the supplementary information.

3.2. Electrical conductivity

Results of the electrical conductivity measurements on the different garnet-type samples are shown in Fig. 4 as function of temperature. Table 1 lists the room temperature conductivities and activation energies of all materials prepared in this study. Within the series of the (Al_2O_3 free) Ta-substituted garnets all samples show higher activation energies compared to LLZO (Table 1). Interestingly, we did not find a significant dependence of the activation energy on the degree of Ta substitution which would correspond to the observed decrease of the lattice parameter a with increasing Ta content as shown in Fig. 3. One might expect that gradually reduced lattice parameters lead to gradually enlarged energy barriers for the lithium movement in the garnet lattice, and thus, growing activation energies. Instead, the activation energies in the series of Ta substituted samples remained unchanged within the limits of their estimated standard deviations. Therefore, we suggest that even small concentrations ($x = 0.5$) of the higher charged Ta^{5+} ion together with the corresponding decrease of the lithium content lead to significant changes in the potential barriers for lithium ion jumps in the cubic garnet-type lattice. A further increase of the Ta content does not significantly influence the energy barriers for the lithium jump processes any more. These results are in agreement with results found for other substitution series of different garnet-type materials [23].

The impact of Ta substitution on the conductivities is somewhat different. Fig. 5 shows the room temperature conductivities of the prepared garnet samples as a function of the Ta content. We found that a small Ta content ($x = 0.5$) leads to a low room temperature conductivity of only 2×10^{-6} S cm^{-1}, which is in agreement with results published for a sample with a Ta content of $x = 0.375$ [10]. For a Ta content corresponding to $x = 1$ we found a comparably high conductivity of 2.6×10^{-4} S cm^{-1}. This is in agreement with results recently published [11], apart from a slightly higher conductivity as well as a slightly higher activation energy for the sample prepared in the present study. With a higher Ta content of $x = 1.5$ the conductivity decreased again to 9×10^{-5} S cm^{-1}. Therefore, the influence of the Ta content on the conductivity cannot simply be related to the number of lithium ions in the garnet-type structure, as we found the conductivity of lithium-poor $Li_{5.5}La_3Zr_{0.5}Ta_{1.5}O_{12}$ was higher than that of lithium-rich $Li_{6.5}La_3Zr_{1.5}Ta_{0.5}O_{12}$. Actually, the conductivity reaches a maximum for a Ta content at about $x(Ta) = 1$ and

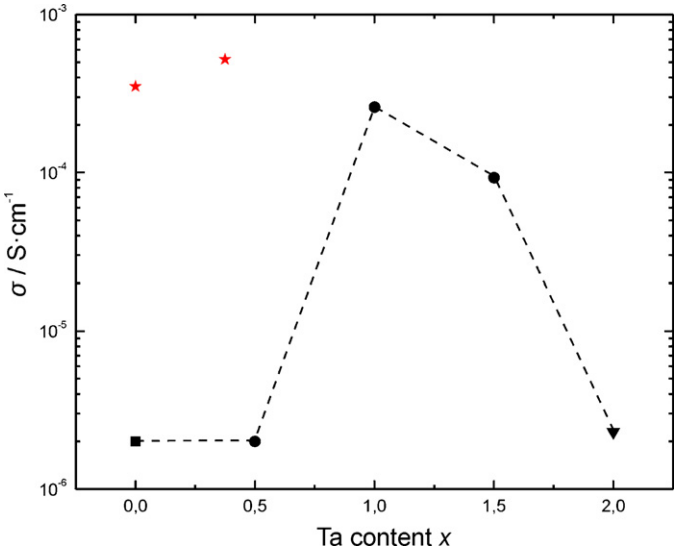

Fig. 5. Dependence of room temperature conductivities on the Ta content x of the prepared garnet-type materials with black symbols (rectangle, circles and triangle) representing Al-free materials and red stars representing Al-doped samples. The value of the black rectangle was taken from Ref. [8] and represents LLZO in the tetragonal modification, the value of the black triangle was taken from Ref. [39].

Table 1
Summary of room temperature conductivities and activation energies as well as exchange current densities and activation energies of the electrode polarization resistance of the prepared garnet-type samples.

Garnet-type material	Conductivity, σ_{25} (S cm^{-1})	Activation energy, E_a (eV)	Exchange current density, i_0 (μA cm^{-2})	Activation energy, E_a (eV)
$Li_{5.5}La_3Zr_{0.5}Ta_{1.5}O_{12}$	9.3×10^{-5}	0.49	–	–
$Li_6La_3ZrTaO_{12}$	2.6×10^{-4}	0.46	46	0.46
$Li_{6.5}La_3Zr_{1.5}Ta_{0.5}O_{12}$	2.0×10^{-6}	0.49	–	–
$Li_{6.625}La_3Zr_{1.625}Ta_{0.375}O_{12}$ (29 mol% Al)	5.2×10^{-4}	0.41	240	0.44
$Li_7La_3Zr_2O_{12}$ (28 mol% Al)	3.5×10^{-4}	0.36	18	0.41

decreases with further increased Ta content as depicted in Fig. 5. Similar behavior is often found for substitution series of garnet-type materials [12,23–25]. Obviously, the Ta content influences lithium disorder and mobility in the garnet-type structure, possibly by affecting lithium site occupancy on 24*d* and 96*h* lithium positions [26]. For detailed insight, further experiments (e.g. neutron diffraction experiments and dynamic Li-NMR studies) are required to clarify the lithium site distributions in the different Ta-substituted samples and its impact on lithium ion conductivity.

Among all prepared samples the 29 mol% Al-doped material with the low Ta content of $x = 0.375$ shows the highest room temperature conductivity of 5.2×10^{-4} S cm^{-1} with an activation energy of $E_a = 0.41$ eV. The Al-doped cubic LLZO prepared for this study shows a conductivity of 3.5×10^{-4} S cm^{-1} and an activation energy $E_a = 0.36$ eV, which is in good agreement with samples prepared before and values known from literature [3,5,6,8]. A systematic study by Yamamura et al. on Ta substitution together with Al doping of LLZO over small Ta contents $0.11 < x < 0.56$ showed a large influence of the sintering atmosphere on the conductivities [10]. In this study by Yamamura et al. a sample with similar composition to our sample shows a conductivity of only $\sim 4 \times 10^{-5}$ S cm^{-1} when sintered in air but a high conductivity of $\sim 8 \times 10^{-4}$ S cm^{-1} when sintered in Ar atmosphere. The oxide powders in this present study have strictly been prepared under air atmosphere in order to suppress the possibility of partial reduction of the samples, which could induce electronic conductivity. We found a significantly higher conductivity for our air sintered sample which is almost comparable to that found for the sample sintered in Ar atmosphere in the aforementioned study by Yamamura et al. We have currently no explanation for this discrepancy but assume that it is caused by different microstructures of the polycrystalline samples. However, it is obvious that Al doping has a significant influence also on the electrical properties of the Ta-substituted garnet-type materials. As known for LLZO [8], we assume that Al causes enhanced lithium disorder and thus lithium ion conductivity by incorporation into the garnet-type structure instead of mainly reducing the grain boundary resistances as supposed in the literature [13]. Fig. 6 shows a Nyquist plot of the room temperature impedance of Al free $Li_6La_3ZrTaO_{12}$ (measured with lithium electrodes pressed on the surfaces). Only one high frequency semicircle representing the total resistance of the sample is observed. The low frequency semicircle represents the electrode (contact) resistance of the lithium/garnet interface. We did not observe any significant contribution of grain boundaries although the pellet was prepared totally free of Al. Nevertheless, the high frequency semicircle might be composed of two interleaved semicircles arising from bulk and grain boundary contributions which could not be resolved in the measurement.

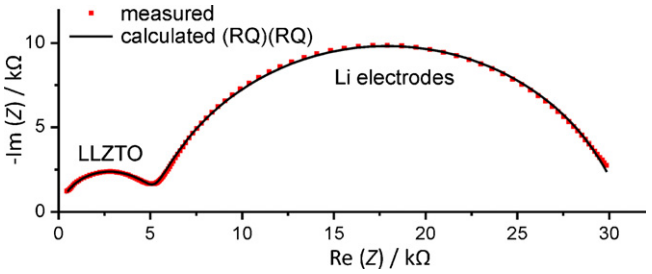

Fig. 6. Nyquist plot of room temperature impedance spectroscopy of a sintered $Li_6La_3ZrTaO_{12}$ pellet measured with lithium electrodes between 7 MHz and 1 Hz with 20 mV amplitude.

3.3. FEM simulations of different electrode arrangements and comparison

For two reasons the use of reference electrodes (RE) in solid electrolyte measurements is more difficult than in the liquid state: First, the use of parent metal or gas electrodes as RE leads only to "pseudo RE". Second, it is laborious if not almost impossible to place a very small RE in front of the working electrode (WE), thereby reducing the *IR* drop caused by the ohmic electrolyte resistance between WE and RE, as it is possible in liquid electrolyte measurements using Haber–Luggin capillaries. Hence, also three electrode measurements need to be corrected for the unavoidable *IR* drop between WE and RE caused by the electrolyte resistance (R_{WE-RE}) between them. This is all the more important for solid electrolytes, as the electrolyte resistances are higher and the distance between WE and RE are usually larger than for measurements in liquid electrolytes. Unfortunately, the correct experimental determination of the electrolyte resistance between RE and WE is cumbersome for solid electrolytes.

In earlier studies of the Li_3N/lithium metal interface kinetics [14,15] the authors determined the resistance R_{WE-RE} by an impedance measurement between WE and RE prior to the current–voltage measurements and used this resistance to correct the current–voltage data. This is a common approach but leads to incorrect results depending on the used electrode arrangement. Consequently, the choice of the proper electrode setup, in particular the position of the RE, has been a subject of intensive discussion e.g. in the field of solid oxide fuel cell electrodes [27–31]. However, for experimental simplification in solid electrolyte studies the RE is typically placed onto the electrolyte surface more or less close to the WE as depicted in Fig. 1(b) and (c) instead of placing it inside the electrolyte bulk just in front of the electrode. Using FEM approach we simulated two different experiments and calculated the current and voltage distributions as well as the resulting resistances R_{WE-RE} for both depicted electrode arrangements: First, we simulated a typical three electrode experiment for both electrode arrangements. Thus, the electric field was applied between WE and CE. The current and voltage distribution and the resulting R_{WE-RE} was calculated. Second, we simulated the impedance measurement between WE and RE. Thus, the electric field was applied between WE and RE. Again, the field distribution and the resulting resistance R'_{WE-RE} were calculated. In order to distinguish this resistance from the "real" resistance R_{WE-RE} controlling the *IR* drop we denote it as R'_{WE-RE}. The graphical visualization of results from the first simulations is presented in Fig. 7(a) and (b).

As expected, a homogeneous electric field results between WE and the CE, with current lines extending into the sample regions

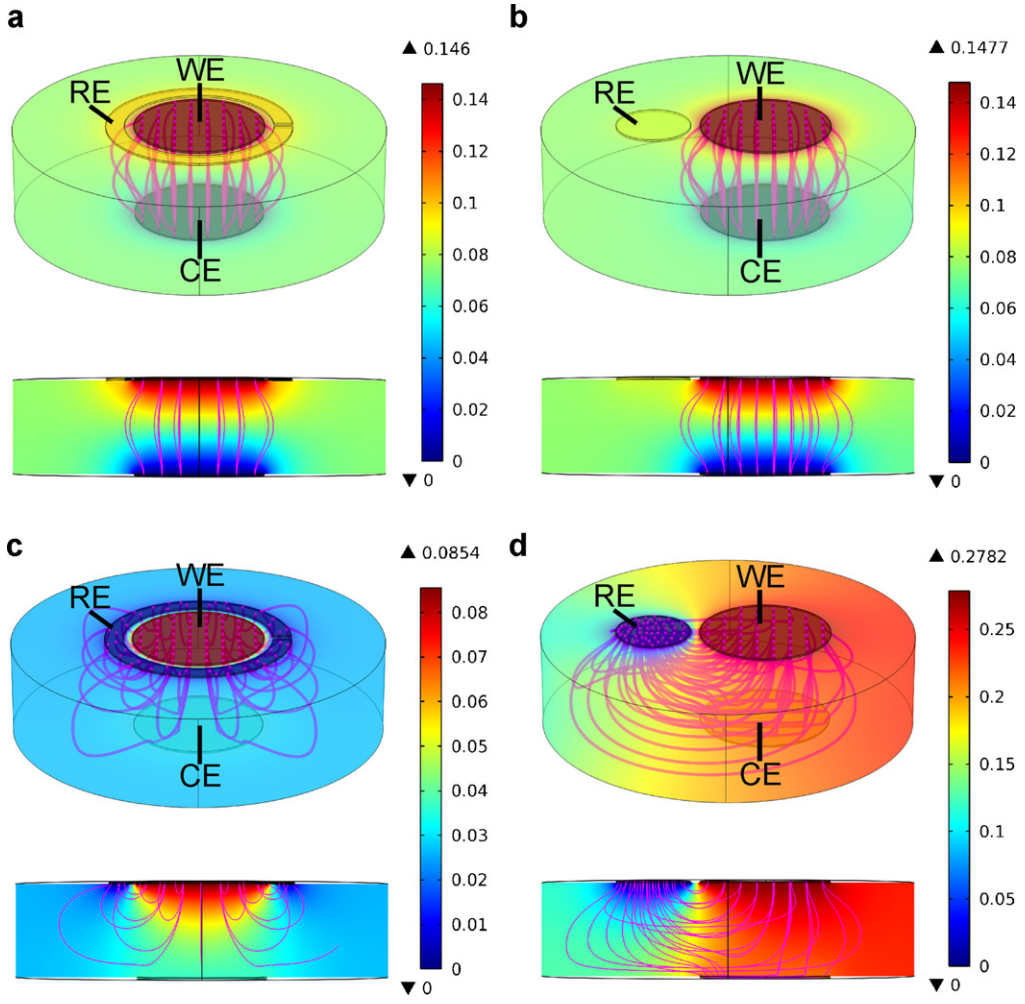

Fig. 7. Finite element method (FEM) simulations of the potential distribution (color code) and lines of equal current densities (red lines) for two different electrode configurations at a simulated current of 100 μA. Pellets diameter and thickness are 20 mm and 5 mm, respectively, diameter of working electrode (WE) and counter electrode (CE) are 7 mm, electrolyte conductivity is 5.2×10^{-4} S cm^{-1}. The color code in the top pictures represents the surface potential distribution while the bottom pictures show the cross section potential distribution. In (a and b) the current is applied between WE and CE, in pictures (c and d) the current is applied between WE and the reference electrode (RE). (For interpretation of the references to color in this figure legend, the reader is referred to the web version of the article.)

which are not covered by both WE and CE. The potential of the RE is visualized by its color. It is affected by the electric field between the WE and CE and is significantly different for the two geometries presented in Fig. 7(a) and (b) although the distance between the WE and RE is 0.5 mm in both simulations. As expected, the shape and position of the RE has a significant effect on the *IR* drop between WE and RE during three electrode measurements. The *IR* drop to the disk shaped RE (Fig. 7(b)) is about 30% higher than to the ring shaped RE (Fig. 7(a)). The numerical results of the FEM simulations are summarized in Table 2.

Fig. 7(c) and (d) shows FEM graphs of the current and voltage distributions for the simulated impedance measurement. Of course, as the current flows between WE and RE, the electric field distribution is quite different from the distribution arising in the simulated three electrode measurement with current flowing between WE and CE. This can be clearly seen by comparing Fig. 7(a) and (c) as well as (b) and (d), respectively. As a matter of fact, the resulting electrolyte resistance R_{WE-RE} actually arising in the three electrode measurements differs significantly from R'_{WE-RE} arising in the impedance measurement. Comparing the calculated results shown in Table 2 it is obvious that the use of R'_{WE-RE} for the *IR* drop correction is incorrect (excluding special geometrical electrode arrangements not shown here).

We like to add that the experimental determination of R_{WE-RE} arising during a three electrode measurement is also possible, but requires laborious sample preparation and careful considerations. The RE has then to be placed for instance in front of the WE within the electrolyte [31]. Alternatively, for cylindrical samples with sufficient thickness a cylindrical RE can be placed in the middle between WE and CE [29]. As working with air sensitive and

Table 2
Summary of calculated results obtained from FEM simulations shown in Fig. 7(a–d).

Electrode arrangement (see Fig. 7)	Simulated measurement conditions	*IR* drop WE to RE (mV)	Resistance WE to RE (Ω)
Fig. 7a	CV with current flow WE to CE	48.5	485
Fig. 7b	CV with current flow WE to CE	62.4	624
Fig. 7c	Impedance with current flow WE to RE	85.4	854
Fig. 7d	Impedance with current flow WE to RE	278	2780

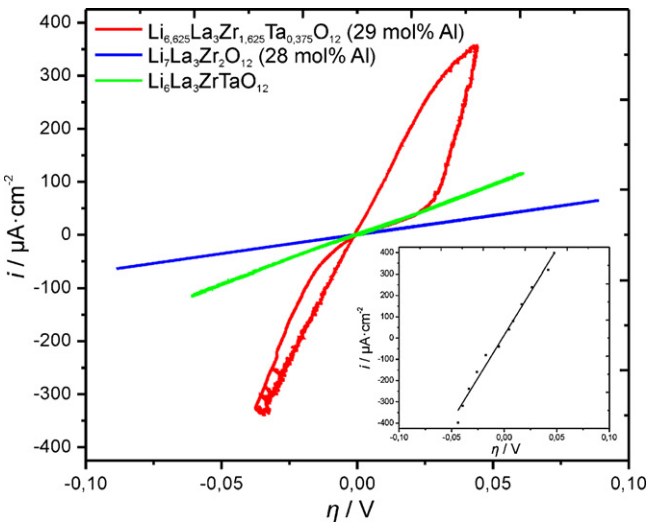

Fig. 8. Cyclic voltammograms at 25 °C of respective garnet-type samples measured between ±0.1 V with a sweep rate of 1 mV s^{-1}. The inset shows the 25 °C current–voltage galvanostatic measurements with the linear fit to the data (solid line) performed on $Li_{6.625}La_3Zr_{1.625}Ta_{0.375}O_{12}$ (29 mol% Al).

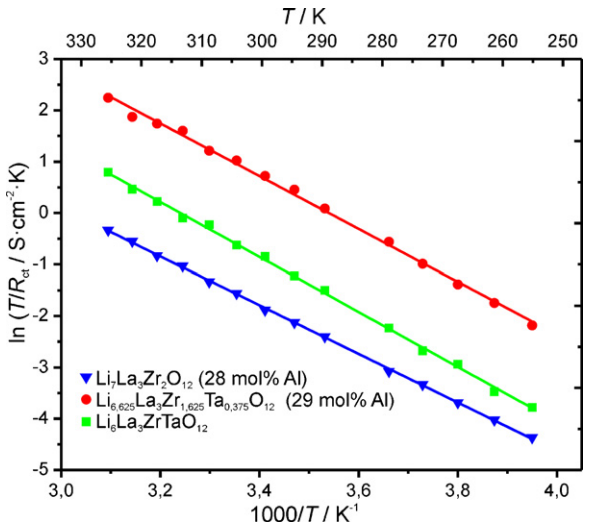

Fig. 9. Arrhenius behavior of the charge transfer resistance at the lithium/garnet interface of different garnet-type materials with the linear fit to the data points (solid lines).

soft lithium metal in a glove-box is a bit cumbersome, this kind of sample preparation proved to be unfavorable. Instead, we used a geometry that is well reproducible by simultaneous gas phase deposition of WE and RE made from lithium metal. Furthermore, the FEM simulations are reliable enough to determine the proper electrolyte resistance R_{WE-RE} between WE and RE. We used the FEM simulations to calculate these values at different temperatures and used them for the *IR* drop correction of the measurements at different temperatures.

3.4. Polarization resistance of the lithium metal/garnet electrode

Measurements of the polarization resistance were performed on those three garnet-type materials showing the highest room temperature conductivities. These were the Al-doped samples $Li_{6.625}La_3Zr_{1.625}Ta_{0.375}O_{12}$ (29 mol% Al) and $Li_7La_3Zr_2O_{12}$ (28 mol% Al) as well as the Al-free $Li_6La_3ZrTaO_{12}$. Temperature dependent current–voltage measurements were performed by CV as described in the experimental section. A low sweep rate of 1 mV s^{-1} was used to achieve quasi steady state conditions. The relatively small voltage range of ±0.1 V was chosen to limit the current flow at the working electrode. It is well known that metal/solid electrolyte interfaces are morphologically unstable under high current densities due to inhomogeneous dissolution and deposition of the metal at the electrolyte metal interface, leading to decreased contact area [16–18,32–35]. To keep these morphological changes small the current flow was kept to the possible minimum. For comparison of the quasi steady state CV measurements with steady state measurements, additional galvanostatic measurements were carried out on the $Li_{6.625}La_3Zr_{1.625}Ta_{0.375}O_{12}$ (29 mol% Al) sample. Steady state galvanostatic measurements were performed between ±400 µA cm^{-2} and the resulting working electrode potential was measured over a period of 30 s per current step. Fig. 8 shows the results of CV measurements together with results of the galvanostatic measurements in the inset. The *IR* drop correction of the measurements was done by FEM simulations as described in the previous section. Measurements were started in cathodic direction to deposit "fresh" lithium at the working electrode. Comparing CV and galvanostatic measurements we noticed no significant differences between the respective results. Therefore, we preferred the faster CV measurements. From the results presented in Fig. 8 we see no difference between anodic and cathodic scans except for the $Li_{6.625}La_3Zr_{1.625}Ta_{0.375}O_{12}$ (29 mol% Al) sample. The deviations arising during the measurement on this material are possibly due to the aforementioned morphological changes at the lithium/garnet interface, since the current density is significantly higher than in measurements on the other garnet-type materials. The otherwise linear behavior indicates the reversibility of the electrode process. Assuming rate control by charge transfer, we can describe the electrode kinetics in the given small voltage range by the linearized Butler–Volmer equation:

$$i = i_0 \frac{F\eta}{RT} \tag{1}$$

where i is the current density, i_0 the exchange current density, F the Faraday constant, η the overvoltage, R the gas constant and T is the absolute temperature. The exchange current densities can be calculated from Eq. (1) replacing i/η by the polarization resistance R_p which can be calculated from the slope of the current–voltage plots as $R_p = (d\eta/di)$

$$i_0 = \frac{RT}{FR_p} \tag{2}$$

The exchange current densities were found to be in the range of 18 µA cm^{-2} up to 240 µA cm^{-2} for the investigated garnet-type materials. These values are in good agreement with values found for the exchange current density at the Li/Li_3N interface of i_0 = 17 µA cm^{-2} and i_0 = 145 µA cm^{-2} at the Li/LiI(Al_2O_3) interface [14,16]. The exchange current densities at 25 °C as calculated from the linear regions of the current–voltage plots shown in Fig. 8 are i_0 = 18 µA cm^{-2} for Al-doped LLZO, i_0 = 240 µA cm^{-2} for $Li_{6.625}La_3Zr_{1.625}Ta_{0.375}O_{12}$ (29 mol% Al) and i_0 = 46 µA cm^{-2} for Al free $Li_6La_3ZrTaO_{12}$. Fig. 9 shows the temperature dependence of the polarization resistance R_p of the garnet-type samples, which is well described by an Arrhenius-type function:

$$\ln\left(\frac{1}{R_p}T\right) = \ln(A) - \frac{E_a}{RT} \tag{3}$$

E_a is the activation energy, T the absolute temperature, R the gas constant and A is the pre-exponential factor. The activation energies calculated from the Arrhenius plots were found to be E_a = 0.41 eV for Al-doped LLZO, E_a = 0.44 eV for $Li_{6.625}La_3Zr_{1.625}Ta_{0.375}O_{12}$ (29 mol% Al) and E_a = 0.46 eV for the Al-free $Li_6La_3ZrTaO_{12}$. The activation energies of R_p are slightly higher (by not more than ~10%) than the activation energies found for the electrical conductivities of

LLZO and $Li_{6.625}La_3Zr_{1.625}Ta_{0.375}O_{12}$ (29 mol% Al) and equal for $Li_6La_3ZrTaO_{12}$. This might be an indication for rate control by ion migration within the garnet phase, i.e. by constriction (or spreading) resistances at the real contact area of lithium metal and electrolyte. A simple "contact loss model" already described by Raleigh [36] and later adopted by Rickert [18] describes the electrode resistance as the sum of the constriction resistances of numerous small contacts which form as a result of the anodic metal dissolution and the formation of voids at the parent metal electrode. Janek and co-workers studied this void formation and the corresponding interface instability in detail at Ag/AgI solid electrolyte interfaces [32–35,37]. A small metal/electrolyte contact leads to a constriction resistance which only depends on the shape and size of the contact area and the ionic conductivity of the electrolyte. Thus, the temperature dependence of the constriction resistance is necessarily similar to the temperature dependence of the bulk electrolyte. As a consequence, the exchange current densities then depend strongly on the interface microstructure and mechanical boundary conditions, which may differ considerably from one experiment to the other. However, we found the exchange current densities to be well reproducible, and therefore the simple contact loss model alone is not sufficient for the interpretation of our results.

Nevertheless, for the large current densities occurring during the measurement on $Li_{6.625}La_3Zr_{1.625}Ta_{0.375}O_{12}$ (29 mol% Al) the interfacial current deviated from a linear current–voltage dependence, most probably due to structural changes of the lithium/garnet interface resulting from a degrading electrode contact by pore formation. Hence, a subject of further studies will be to investigate the electrode kinetics under varying electrode contact pressures. Increased contact pressures may help to improve the contact under current flow, thus leading to steady currents under higher polarization voltages [17]. In fact, the anodic electrode process at the lithium/garnet interface is a combination of the lithium transfer across the interface as well as the simultaneous formation of a vacancy in the metal surface and the incorporation of a lithium ion into the garnet structure. We are not aware of theoretical concepts for the estimation of activation barriers for these interface processes at parent metal electrodes on solid electrolytes. Therefore, additional experimental data are required to expand the data basis for electrode processes as well as theoretical studies to obtain deeper understanding of the rate limiting steps.

4. Conclusions

We successfully synthesized tantalum substituted phases of the well known cubic garnet-type solid electrolyte "$Li_7La_3Zr_2O_{12}$" with different Ta content. The Ta substituted analogues with the nominal formula $Li_{7-x}La_3Zr_{2-x}Ta_xO_{12}$ were found to crystallize in the known cubic garnet symmetry (space group $Ia\bar{3}d$) over a wide range of Ta content $x = 0.375–1.5$. The incorporation of Ta into the cubic garnet structure is accompanied by a linear decreasing lattice parameter with increasing Ta content. We found that Al doping is not necessary to achieve good sintering and dense samples of the cubic $Li_{7-x}La_3Zr_{2-x}Ta_xO_{12}$ phases. By Ta substitution the synthesis as well as the sintering temperature of the cubic garnet-type materials could be reduced to 1000 °C, no matter whether Al was present during the synthesis or not. Nevertheless, Al doping was found to improve the conductivity of a sample with low Ta content $Li_{6.625}La_3Zr_{1.625}Ta_{0.375}O_{12}$ (29 mol% Al). This material shows the highest room temperature conductivity of the investigated materials which was 50% higher compared to Ta-free $Li_7La_3Zr_2O_{12}$ (28 mol% Al). We studied the lithium/garnet interface kinetics of the most conductive materials by CV and used FEM simulations to evaluate the *IR* drop and corrected the experimental results accordingly. We also showed that the experimental correction of the *IR* drop by impedance measurements, which is a common approach, leads to erroneous results if the electrode setup is not carefully chosen. From the measurement of the interfacial resistance R_p we found that the Ta-substituted samples show higher exchange current densities than Ta-free LLZO. The $Li_{6.625}La_3Zr_{1.625}Ta_{0.375}O_{12}$ (29 mol% Al) material shows a more than tenfold higher exchange current density of $i_0 = 240\ \mu A\ cm^{-2}$ compared to LLZO. The activation energies for interface and bulk transport are quite close and we discussed rate control by constriction resistances at small contact points between electrode and electrolyte as one possible reason for this fact.

From the results we conclude that a small Ta-content together with Al-doping is a promising way to improve the properties of LLZO. By doing so, the synthesis temperature could be reduced and the room temperature ionic conductivity was increased. We emphasize that the interface resistance at the lithium/garnet interface is reduced about tenfold comparing $Li_{6.625}La_3Zr_{1.625}Ta_{0.375}O_{12}$ (29 mol% Al) and LLZO. Considering the electrolyte together with the interface resistance we can state that by using $Li_{6.625}La_3Zr_{1.625}Ta_{0.375}O_{12}$ (29 mol% Al) instead of LLZO as electrolyte in solid electrolyte cells using lithium metal anodes, the cell resistance can be reduced more than tenfold. The interface resistance of the garnet materials in contact with different cathode materials is also of great importance and therefore a subject of ongoing studies.

Acknowledgments

We acknowledge financial support by the German Research Foundation (DFG) within the project "High performance lithium batteries" (DFG JA 648/15-1 and 15-2). Furthermore, financial support by the Federal Ministry of Education and Research (BMBF) within the project "Competence in Electrochemistry for Electromobility" is gratefully acknowledged. We also acknowledge financial support and fruitful discussions within the BASF Research Network for Batteries and Electrochemistry.

Appendix A. Supplementary data

Supplementary data associated with this article can be found, in the online version, at doi:10.1016/j.jpowsour.2012.01.094.

References

[1] Y. Xiaohua, J.B. Bates, G.E. Jellison, F.X. Hart, J. Electrochem. Soc. 144 (1997) 524–532.
[2] J. Schwenzel, V. Thangadurai, W. Weppner, J. Power Sources 154 (2006) 232–238.
[3] R. Murugan, V. Thangadurai, W. Weppner, Angew. Chem. Int. Ed. 46 (2007) 7778–7781.
[4] C.A. Geiger, E. Alekseev, B. Lazic, M. Fisch, T. Armbruster, R. Langner, M. Fechtelkord, N. Kim, T. Pettke, W. Weppner, Inorg. Chem. 50 (2011) 1089–1097.
[5] Y. Jin, P.J. McGinn, J. Power Sources 196 (2011) 8683–8687.
[6] S. Kumazaki, Y. Iriyama, K.-H. Kim, R. Murugan, K. Tanabe, K. Yamamoto, T. Hirayama, Z. Ogumi, Electrochem. Commun. 13 (2011) 509–512.
[7] M. Kotobuki, K. Kanamura, Y. Sato, T. Yoshida, J. Power Sources 196 (2011) 7750–7754.
[8] H. Buschmann, J. Dölle, S. Berendts, A. Kuhn, P. Bottke, M. Wilkening, P. Heitjans, A. Senyshyn, H. Ehrenberg, A. Lotnyk, V. Duppel, L. Kienle, J. Janek, Phys. Chem. Chem. Phys. 13 (2011) 19378–19392.
[9] R. Murugan, S. Ramakumar, N. Janani, Electrochem. Commun. (2011) 1373–1375.
[10] Y. Yamamura, T. Hattori, T. Yoshida, A. Honda, Y. Sato, United States Pat., US 20,110,053,002 A1 (2011).
[11] Y. Li, C.-A. Wang, H. Xie, J. Cheng, J.B. Goodenough, Electrochem. Commun. (2011) 1289–1292.
[12] S. Ohta, T. Kobayashi, T. Asaoka, J. Power Sources 196 (2011) 3342–3345.
[13] H. Xie, J.A. Alonso, Y. Li, M.T. Fernaïndez-Diïaz, J.B. Goodenough, Chem. Mater. 23 (2011) 3587–3589.
[14] U. von Alpen, M.F. Bell, Solid State Ionics 3 (4) (1981) 259–262.
[15] M.F. Bell, U. von Alpen, J. Electroanal. Chem. 129 (1981) 315–319.

[16] T.R. Jow, C.C. Liang, J. Electrochem. Soc. 130 (1983) 737–740.
[17] T.R. Jow, C.C. Liang, Solid State Ionics 9–10 (1983) 695–698.
[18] M. Meyer, H. Rickert, U. Schwaitzer, Solid State Ionics 9–10 (1983) 689–693.
[19] J. Rodriguez-Carvajal, Commission Powder Diffract. Newslett. 26 (2001) 12–19.
[20] J. Rodriguez-Carvajal, Physica B 192 (1993) 55–69.
[21] R.D. Shannon, C.T. Prewitt, Acta Crystallogr. B 25 (1969) 925–946.
[22] R.D. Shannon, Acta Crystallogr. A 32 (1976) 751–767.
[23] M.P. O'Callaghan, A. Powell, J. Titman, G. Chen, E.J. Cussen, Chem. Mater. 20 (2008) 2360–2369.
[24] R. Murugan, V. Thangadurai, W. Weppner, Ionics 13 (2007) 195–203.
[25] R. Murugan, V. Thangadurai, W. Weppner, Appl. Phys. A 91 (2008) 615–620.
[26] A. Logéat, T. Köhler, U. Eisele, B. Stiaszny, A. Harzer, M. Tovar, A. Senyshyn, H. Ehrenberg, B. Kozinsky, Solid State Ionics 206 (2012) 33–38.
[27] S.B. Adler, J. Electrochem. Soc. 149 (2002) E166.
[28] S.B. Adler, B.T. Henderson, M.A. Wilson, D.M. Taylor, R.E. Richards, Solid State Ionics 134 (2000) 35–42.
[29] J. Rutman, I. Riess, Electrochim. Acta 52 (2007) 6073–6083.
[30] J. Rutman, I. Riess, Solid State Ionics (2008) 108–112.
[31] J. Winkler, P.V. Hendriksen, N. Bonanos, M. Morgensen, J. Electrochem. Soc. 145 (1998) 1184–1192.
[32] J. Janek, Solid State Ionics 131 (2000) 129–142.
[33] J. Janek, S. Majoni, Ber. Bunsenges. Phys. Chem. 99 (1995) 14–20.
[34] H. Schmalzried, J. Janek, Ber. Bunsenges. Phys. Chem. 102 (2) (1998) 127–762.
[35] S. Majoni, J. Janek, Ber. Bunsenges. Phys. Chem. 102 (5) (1998) 756–762.
[36] D.O. Raleigh, Electroanal. Chem. 6 (1972) 87–186.
[37] S. Majoni, J. Janek, Solid State Ionics 85 (1996) 247–250.
[38] D. Mazza, Mater. Lett. 7 (1988) 205–207.
[39] V. Thangadurai, H. Kaack, W.J.F. Weppner, J. Am. Ceram. Soc. 86 (2003) 437–440.